

**Pierluigi Pagliaro**  
Dipartimento di Meccanica,  
Università degli Studi di Palermo,  
90128 Palermo, Italy  
e-mail: pagliaro@dima.unipa.it

**Michael B. Prime**  
e-mail: prime@lanl.gov

**Bjørn Clausen**

**Manuel L. Lovato**

Los Alamos National Laboratory,  
Los Alamos, NM 87544

**Bernardo Zuccarello**  
Dipartimento di Meccanica,  
Università degli Studi di Palermo,  
90128 Palermo, Italy

# Known Residual Stress Specimens Using Opposed Indentation

*In order to test new theories for residual stress measurement or to test the effects of residual stress on fatigue, fracture, and stress corrosion cracking, a known stress test specimen was designed and then fabricated, modeled, and experimentally validated. To provide a unique biaxial stress state, a 60 mm diameter 10 mm thick disk of 316L stainless steel was plastically compressed through the thickness with an opposing 15 mm diameter hard steel indenters in the center of the disk. For validation, the stresses in the specimen were first mapped using time-of-flight neutron diffraction and Rietveld full pattern analysis. Next, the hoop stresses were mapped on a cross section of two disks using the contour method. The contour results were very repeatable and agreed well with the neutron results. The indentation process was modeled using the finite element method. Because of a significant Bauschinger effect, accurate modeling required testing the cyclic behavior of the steel and then modeling it using a Chaboche-type combined hardening law. The model results agreed very well with the measurements. The duplicate contour measurements demonstrated stress repeatability better than 0.01% of the elastic modulus and allowed discussion of implications of measurements of parts with complicated geometries. [DOI: 10.1115/1.3120386]*

**Keywords:** residual stress, contour method, neutron diffraction

## 1 Introduction

Residual stresses play a significant role in many material failure processes such as fatigue, fracture, stress corrosion cracking, buckling, and distortion [1]. Residual stresses are the stresses present in a part free from any external load, and they are generated by virtually any manufacturing process. Because of their important contribution to failure and their almost universal presence, the knowledge of residual stress is crucial for prediction of the strength of any engineering structure. However, the prediction of residual stresses is a very complex problem. In fact, the development of residual stress generally involves nonlinear material behavior, phase transformation, coupled mechanical and thermal problems, and/or varying mechanical properties throughout the material. Hence, the ability to accurately quantify residual stresses through measurement is an important engineering tool.

A hypothesized improvement to the contour method that needs experimental validation motivated this study to produce a novel test specimen. In the literature there are many residual stress measurement techniques. Each of them has its advantages and disadvantages, and its own accuracy. The recently developed contour method is one of the few methods that can measure a 2D map of internal stresses, and it can be applied to many parts that are difficult for other methods [2–8]. As originally presented, the contour method only measured the stress component normal to the cross section of measurement. More recent extensions to the contour method [9,10] determine multiple components using multiple cuts. However, in theory one should be able to measure multiple components with a single cut if subsequent measurements are taken on the cut surface with other techniques. A test specimen with significant stresses in two directions that were also significantly different from each other would provide the most convincing validation of the new theory. Since both the new theory and

the independent validation would require other measurement methods, the specimen would have to be possible to measure with multiple techniques.

Another important use for known stress specimens is to experimentally test the effects of residual stress on fatigue, fracture, creep, stress corrosion cracking, or other material behavior [11].

Most common residual stress test specimens are not ideal for the required validation purposes. Various procedures for introducing residual stresses into a test specimen have been used. The most common is a plastically bent beam producing a typical zig-zag residual stress distribution through the thickness [12,13]. However, a bent beam produces only uniaxial stresses, which are not satisfactory for this validation. Other common validation specimens are based on producing multiple specimens identically with a stress inducing process such as peening and then measuring the stresses with some other technique. A specimen with stresses that could be easily predicted or modeled would provide the additional benefit of not requiring extensive independent measurements.

This paper presents the design, the fabrication, the material characterization, and the finite element (FE) prediction of the residual stresses of the specimen described in the earlier paragraph. Furthermore, in order to measure the residual stress field produced with this technique, a neutron diffraction experiment was executed on this specimen. Then the contour method was applied to two different test specimens—the specimen and a virtually identical second specimen—and it was possible to verify its good repeatability.

## 2 Specimen Design

A test specimen was designed to provide a residual stress distribution particularly well suited for a specific experimental validation. It was desired to validate the multiple-component contour method on different stress states where the two significant normal stress components were approximately equal (i.e., equibiaxial) and, conversely, of opposite sign. Such stress states can be produced in a single shrink-fit ring and plug, in which the expansion of a cooled oversized plug is constrained by a surrounding ring

Contributed by the Materials Division of ASME for publication in the JOURNAL OF ENGINEERING MATERIALS AND TECHNOLOGY. Manuscript received June 17, 2008; final manuscript received October 11, 2008; published online May 21, 2009. Assoc. Editor: Hussein Zbib.

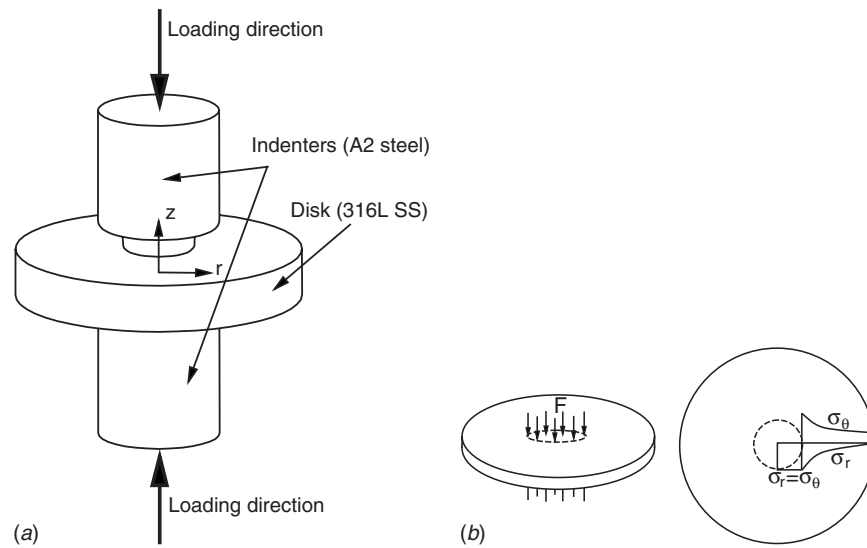


**Fig. 1 Schematic illustrating (a) the indentation process and (b) the conceptual residual stress distribution obtained**

resulting in biaxial compressive residual stresses in the plug. The ring experiences compressive radial stresses under the forces from the plug, but the hoop stresses are tensile.

Since a real ring and plug would fall apart during contour method cutting, an alternative configuration to produce a similar residual stress distribution was used. A circular disk was plastically compressed through the thickness by two cylindrical indenters of smaller diameter (see Fig. 1(a)). A similar specimen was recently used to study fatigue and fracture behavior [11]. The compressed region between the two indenters yields and wants to expand in the radial direction due to the Poisson effect. Under the constraint of the surrounding material, analogous to the ring in the example of a shrink-fit ring and plug, a biaxial (hoop and radial) compressive residual stress state is produced in the central region, while in the outer region there will be tensile and compressive residual stresses for hoop and radial stresses, respectively (see Fig. 1(b)). Obviously, the real residual stress field will be continuous and not discontinuous like in the shrink-fit ring and plug, because in this case we have only one part.

The geometry of the specimen was then designed considering the material behavior and experimental limitations. A 60 mm diameter 10 mm thick disk was chosen with the indenters 15 mm in diameter (see Fig. 2). The thickness was chosen based on the limited penetration of neutrons through steel. The diameters of the disk and the indenters were chosen to obtain stress gradients that could be resolved using reasonable neutron sampling volumes and to obtain a relaxed contour of at least 20  $\mu\text{m}$  (peak-to-valley) for

the contour method measurement, considering the maximum load of the test machine (100 kN). Furthermore, the shape of the indenters was designed to reduce the stress concentration due to sharp corners. To optimize the design for these considerations, several preliminary finite element simulations of the indentation process were carried out. The indenter material used was an A2 tool steel, characterized by a high hardness (58 HRC) and a high yield stress (about 1300 MPa). The Young modulus of the A2 tool is 204 GPa and Poisson's ratio is 0.3. In order to center the two indenters with respect to the disk, two polymethyl methacrylate (PMMA) rings were designed (see Fig. 2), which are moved out of the way prior to indentation.

### 3 Materials

316L stainless steel was chosen for the material as the best compromise among the ideal materials for the different measurement methods that will be required to validate the multiple stress component theories. For the contour method, hole drilling, and other relaxation methods, it is generally better to have a material with high  $S_y/E$  in order to obtain more relaxation. In general, the material yield strength  $S_y$  limits the residual stress magnitudes. An aluminum alloy would be a good choice ( $S_y/E$  can easily exceed 4000  $\mu\epsilon$ ), but, unfortunately, it is usually not as good for X-ray diffraction measurements. Austenitic steel has a lower  $S_y/E$  ( $\approx 950 \mu\epsilon$ ), which means lower relaxed strains, but it is very good for neutron diffraction and X-ray diffraction. 316L stainless steel was chosen based on previous successful diffraction measurements and industrial importance. The disk was machined from a hot cross-rolled plate (457 mm  $\times$  457 mm and 12.7 mm thickness) of 316L stainless steel. The chemical composition of the 316L stainless steel is in weight percent: C=0.018, Mn=1.59, P=0.031, S=0.005, Si=0.23, Ni=10.64, Cr=16.65, Mo=2.16, N=0.05 and Fe=balance (in accord with the ASTM A240 and ASME SA-240).

To have the residual stress produced only by indentation, the material must be initially stress-free. For this reason, the plate was annealed at 1050°C for 30 min in vacuum and then slow cooled to room temperature in argon in order to remove any pre-existing residual stresses. Then, to verify the absence of any pre-existing residual stresses, a slitting method test [14] was executed. A square specimen (60  $\times$  60  $\times$  12.7 mm<sup>3</sup>) was extracted from the annealed plate and was instrumented with two strain gages type CEA-09-032UW-120, aligned along the rolling  $x$ -direction on the

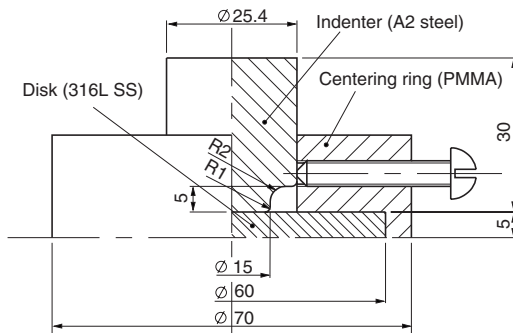


**Fig. 2 Quarter-symmetry drawing of the indentation fixture, dimensions in mm: R1=1 mm and R2=3 mm**

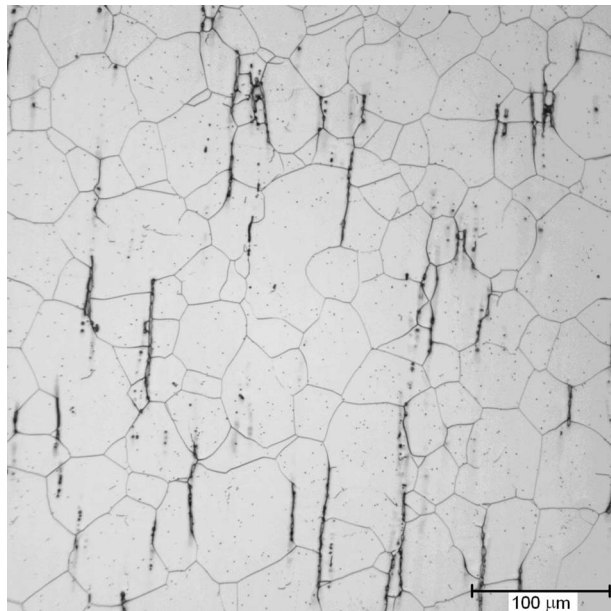


**Fig. 3 Metallography of the 316L plate after annealing, taken normal to one of the rolling directions; the scale bar is 100  $\mu\text{m}$  long**

bottom surface. The cut was executed starting from the opposite surface (top) in 0.38 mm increments to a depth of 12.57 mm, using a wire electric discharge machine (EDM) with a 250  $\mu\text{m}$  brass wire. The original residual stress was determined from the measured strains using the regularized pulse method [15]. The resulting stress magnitudes were lower than 10 MPa, confirming the effectiveness of the annealing process.

After annealing, a metallographic analysis was made on the plate to check the grain-size (see Fig. 3), whose average is about 50–100  $\mu\text{m}$ , with some smaller grains. The metallography also revealed the presence of about 0.5% of ferrite, seen as dark stringers, which is not enough to cause any multiphase problems with the neutron diffraction measurements of residual strains. A small amount of ferrite is typical in 316L stainless.

Constitutive data were required in order to model the material response during the indentation process. For this reason several compression tests, in accord with ASTM standard, were carried out in order to test the mechanical behavior of the material in the through-thickness direction and in the two in-plane directions. Cylindrical specimens, 9.5 mm in diameter and 12.7 mm height, were extracted from the plate. Displacement-control compression tests with a crosshead speed of 0.046 mm/min were executed until  $\sim 20\%$  of engineering strain and were then unloaded. The displacement was measured using a compression extensometer with its arms mounted between the platens. The rate was chosen to give approximately the same strain rate as the one expected during the specimen indentation ( $\dot{\epsilon} = 5 \times 10^{-5} \text{ s}^{-1}$  after correcting for machine compliance). Figure 4 shows the true stress-true strain curves for the three tested material directions. The three curves are very close until the strain exceeds 5%. Considering that except for very localized regions at the indenter edge, the plastic strains from indentation are less than 2%; the material is taken as behaving isotropically. From the slope of the linear part (unloading) of these curves, Young's modulus  $E$  was found to be 193 GPa while the yield stress  $S_y$  is 208 MPa (0.2% offset yield strength). The linear part of the curve during loading gave Young's modulus lower than the expected value for this steel. However, after few consecutive load-unload cycles in the elastic range, the linear loading curve rose to the expected value. Probably, the annealing process resulted in some plasticity at very low loads.

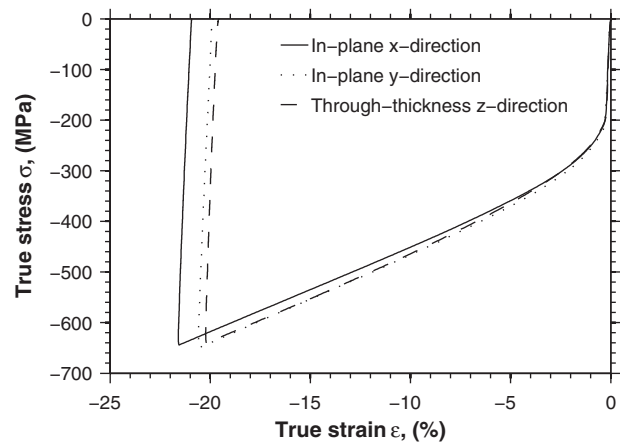


**Fig. 4 True stress-true strain curves of uniaxial compression tests for the 316L stainless steel along the three material directions**

Although not originally planned, cyclic stress-strain curves were also measured in order to accurately model the specimens. Preliminary FE simulation of the indentation process showed that the predicted residual stress field is affected, besides, by the plastic behavior during loading and also by the hardening model for unloading. In fact, the 316L stainless steel exhibits a strong Bauschinger effect [16,17], and, furthermore, the indentation process produces some reverse loading in the central region. Hence, in order to calibrate a hardening model for the FE simulation, cyclic compression and tension tests were performed. Two specimens were extracted from each in-plane material direction of the 316L stainless steel plate. The specimens were 69.85 mm long with a diameter of 5.08 mm and a gauge length of 15.24 mm with threaded ends. Because of the small plate thickness, no cyclic specimens were made in the through-thickness direction. Since the preliminary FE simulations showed that the maximum equivalent plastic strain in the central region of the disk under the indenters was approximately 2%, symmetric controlled strain cyclic tests were executed with a strain range  $\Delta\epsilon$  of 4% (i.e., maximum strain of 2%). A strain rate of  $4.5 \times 10^{-5} \text{ s}^{-1}$  was used, which is the same as that which occurs in the majority of the disks during the indentation. The true stress-true strain curve of one cyclic test is shown in Fig. 5 together with the FE isotropic, kinematic, and

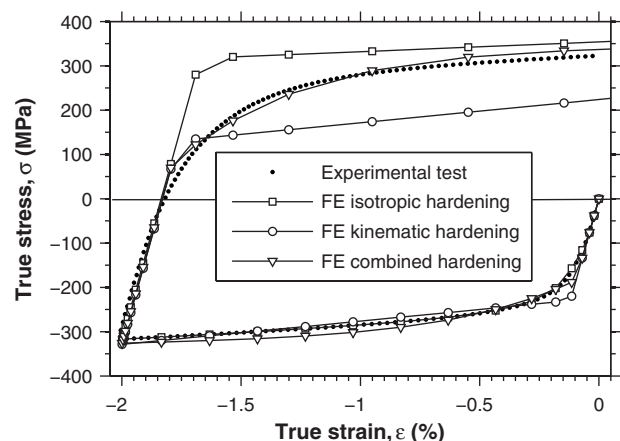


**Fig. 5 Hardening behavior of the 316L in a uniaxial compression and tension together with the FE combined hardening model**

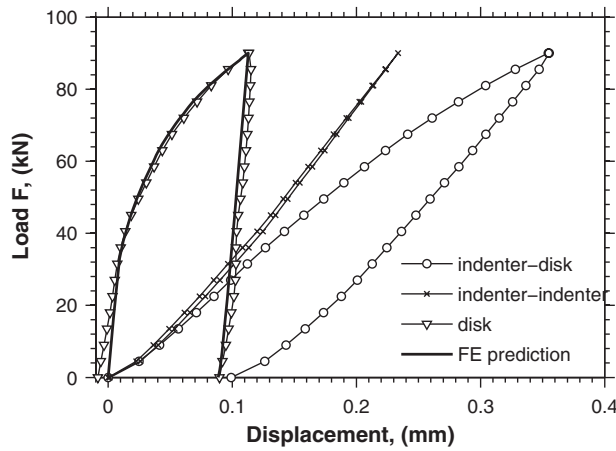


Fig. 6 Load-displacement curves of the indentation process of the 316L SS disk and its FE prediction

combined hardening models that were calibrated on this test and are described in Sec. 5. There was no significant difference in the cyclic test in the other in-plane direction.

#### 4 Indentation Tests

Several disks of 316L stainless steel were indented in the same experimental conditions in order to get virtually the same residual stress field. An Instron 1125 testing machine was used, and the displacement of the punch of the machine were measured with a Keyence magnetic sensor. The specimens were indented to a peak load of 90 kN under displacement control using a crosshead speed of 0.15 mm/min. A MOLYCOTE® antifriction coating was applied on the contact surfaces of the two indenters. The relative alignment of the indenters with respect to the rolling directions of the 316L was kept the same for the indentations of all the specimens. After the test, a footprint in both sides of the disk was produced with a thickness reduction of  $-0.85\%$ .

Since the displacement measurement (circle-line in Fig. 6) is affected by the compliance of the specimen, the indenters, the lubricant, and part of the test machine, due to the position of the displacement sensor, a preliminary test without any specimen (indenter versus indenter) was executed at the same maximum load to measure the in series compliance of the indenters-lubricant-test machine system (x-line in Fig. 6). By subtracting the measured displacements of the two tests, the displacements at the indenter-specimen interface were obtained (triangle-line in Fig. 6). The curves for the various indentations of different disks in the same experimental conditions varied by  $\pm 0.005$  mm. Figure 6 also shows the prediction of the load-displacement curve obtained with a FE simulation of the indentation process, which will be described in Sec. 5.

#### 5 Modeling

The residual stress field produced by the indentation was simulated using the ABAQUS® finite element code [18]. A half-symmetry axisymmetric model of the specimen was built using 15,000 four-node quadrilateral elements (CAX4R) with reduced integration. Square elements 0.1 mm on a side gave a  $50 \times 300$  mesh in the disk. The indenter was modeled using the same element type but with a coarser mesh of 8725 elements of approximately 0.2 mm on a side. Figure 7 shows the FE model. The contact behavior between the indenter (master surface) and the disk (slave surface) was assumed frictionless because lubricant was used during the experimental test and a surface-to-surface contact algorithm was used. Axisymmetric boundary conditions were imposed along the axis of the indenter and the specimen, while symmetric boundary conditions were imposed on the

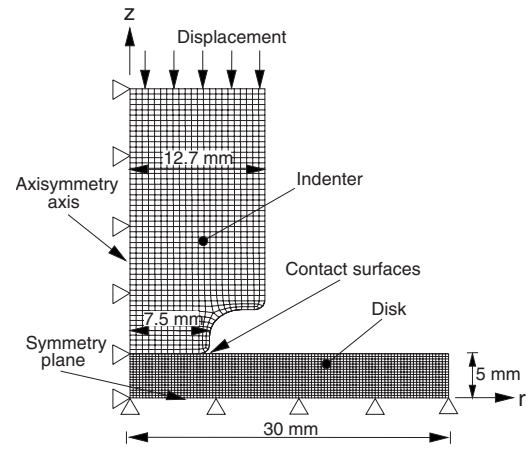


Fig. 7 Details of the axial-symmetric finite element model used showing the planes of symmetry

middle plane of the specimen. A displacement of  $-0.09$  mm in the  $z$ -direction was applied at the upper face of the indenter (the actual cross-head displacement is the double due to the symmetry) in order to achieve the experimentally applied load of  $-90$  kN.

Initial model comparisons with measured residual stresses revealed that a more accurate material hardening model was needed in order to obtain satisfactory agreement. The behavior of 316L stainless steel was initially modeled using an isotropic and a kinematic hardening model, both calibrated on the compression-only experimental data. The indentation load-displacement curves, like in Fig. 6, obtained from the FE analysis for both isotropic and kinematic hardenings do not exhibit any noticeable difference, except a little difference during the unload for less than 10 kN. However, both models gave a poor prediction of the stresses in the indented disk when compared with experiments. These models were then calibrated on the cyclic data by running FE analysis on a simple one element model, subjected to a uniaxial compression of  $-2\%$  of true strain in the first step, followed by a tensile strain of  $2\%$  in the second step. As response, the isotropic hardening predicted higher tensile stress than the experimental data after reverse loading (see Fig. 5), while the kinematic model gave a lower stress. The predicted residual stress obtained using these two hardening models are shown in Fig. 8. It is evident that the different hardening models affect the residual stress because of reverse loading.

Since the experimental data from the cyclic test are in between the isotropic and kinematic hardening models (see Fig. 5), a combined hardening model that involves a kinematic term and an isotropic one in its formulation was used. In detail, the combined hardening model provided by ABAQUS® [19] was used. This hardening model is based on the work of Lemaitre and Chaboche [16]. The pressure independent yield surface is defined by

$$F = f(\boldsymbol{\sigma} - \boldsymbol{\alpha}) - \sigma^0 = 0 \quad (1)$$

where  $\sigma^0$  is the size of yield surface and  $f(\boldsymbol{\sigma} - \boldsymbol{\alpha})$  is the equivalent von Mises stress with respect to the back-stress tensor  $\boldsymbol{\alpha}$ , which is defined by

$$f(\boldsymbol{\sigma} - \boldsymbol{\alpha}) = \sqrt{\frac{3}{2}(\mathbf{S} - \boldsymbol{\alpha}^{\text{dev}}):(\mathbf{S} - \boldsymbol{\alpha}^{\text{dev}})} \quad (2)$$

where  $\mathbf{S}$  is the deviatoric stress tensor,  $\boldsymbol{\alpha}^{\text{dev}}$  is the deviatoric part of the back-stress tensor, and the symbol  $(:)$  is the double contracted product.

The isotropic hardening behavior of the model defines the evolution of the yield surface size  $\sigma^0$  as a function of the equivalent plastic strain  $\bar{\epsilon}^{\text{pl}}$ .



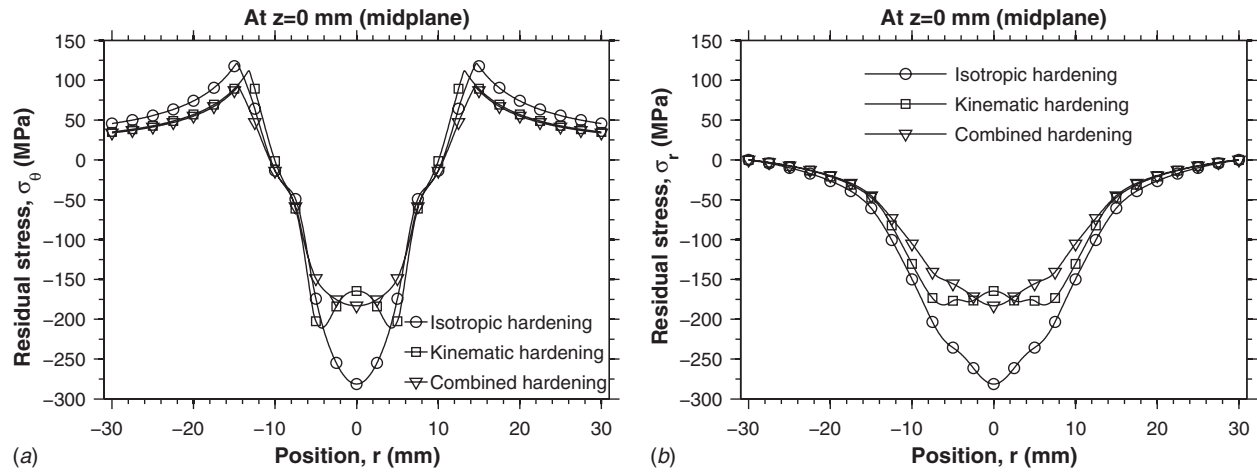


Fig. 8 Finite element model prediction of (a) hoop and (b) radial residual stresses along the mid-thickness line using isotropic, kinematic, and combined hardening models of the 316L stainless steel

$$\sigma^0 = \sigma_0 + Q(1 - e^{-b\bar{\epsilon}^{pl}}) \quad (3)$$

where  $\sigma_0$  is the yield stress at zero plastic strain, and  $Q$  and  $b$  are material parameters. The nonlinear kinematic hardening component is defined by an additive combination of a linear term and a relaxation term, which introduces the following nonlinearity:

$$\dot{\alpha} = \frac{C}{\sigma_0}(\sigma - \alpha)\dot{\bar{\epsilon}}^{pl} - \gamma\alpha\dot{\bar{\epsilon}}^{pl} \quad (4)$$

The parameters for this combined hardening model were calibrated from the cyclic test described before using the procedure described in [18] and their values are:  $\sigma_0 = 185$  MPa,  $C = 28722$  MPa,  $\gamma = 230.7$ ,  $Q = 100$  MPa, and  $b = 12$ .

The indenter material (A2 tool steel) was modeled by assuming linear elastic behavior, since the stresses do not approach yield, which is more than 1300 MPa, during indentation.

The load-displacement curve obtained from the FE analysis considering the combined hardening model is shown in Fig. 6. Figure 8 shows the comparison of the FE prediction of the hoop and radial stress due to indentation using the isotropic, kinematic, and combined hardening model respectively. The stresses under the indenter are quite sensitive to the hardening model because of significant reverse plasticity.

Figure 9 shows the contour maps of the radial, hoop, and axial residual stresses modeled using the combined hardening model that better simulates the 316L stainless steel. Figure 9(c) also shows the region where the reverse plasticity is more than 0.001 (0.1%) (cross hatched region).

## 6 Neutron Diffraction Experiment

Stress maps were measured using the SMARTS instrument at the Los Alamos Neutron Science Center (LANSCE). LANSCE is a pulsed neutron source where each pulse contains a spectrum of wavelengths and is moderated by passing through a chilled water moderator at 10°C. The incident flight path on SMARTS is 31 m, most of it in a neutron guide. SMARTS has two detector banks at  $\pm 90$  deg to the incident beam with a diffracted flight path length of about 1.5 m (see Fig. 10(a)). The total flight path, the scattering geometry, and the 20 Hz repetition rate of the source dictate that the useable wavelength range on SMARTS is about 0.4–3.8 Å with maximum intensity between 0.5 to 1.5 Å.

Strains were measured along the three principal directions at 123 gauge volumes, which locations are shown in Fig. 11, spaced by 1.7 mm from each other in the central part (for  $-15.3$  mm  $\leq r \leq 15.3$  mm) in order to better follow the high strain gradient in the central region of the disk and 3.4 mm elsewhere. Because of limited experimental time, Fig. 11 reflects that the full intended

grid was not measured in all quadrants of the cross section. The incident slits were set to  $2 \times 2$  mm<sup>2</sup>, and a set of radial collimators limited the gauge volume to 2 mm along the incident beam path. The disk was positioned so that the scattering vector for the +90 deg bank  $Q_1$  was along the axial ( $z$ ) direction, and the scattering vector for the -90 deg bank,  $Q_2$ , was along the radial ( $r$ ) direction of the disk. A series of measurements were made on a cross section through the center. Then the disk was rotated 90 deg around the axial  $z$  direction, and another scan was performed in the vertical direction (out of the plane of the paper in Fig. 10(a)). The first and second scans were made in the same physical positions within the disk, but in the first scan the radial strains  $\epsilon_r$  were measured in the -90 deg bank, and in the second scan the hoop strains  $\epsilon_\theta$  were measured in the -90 deg detector bank. In both

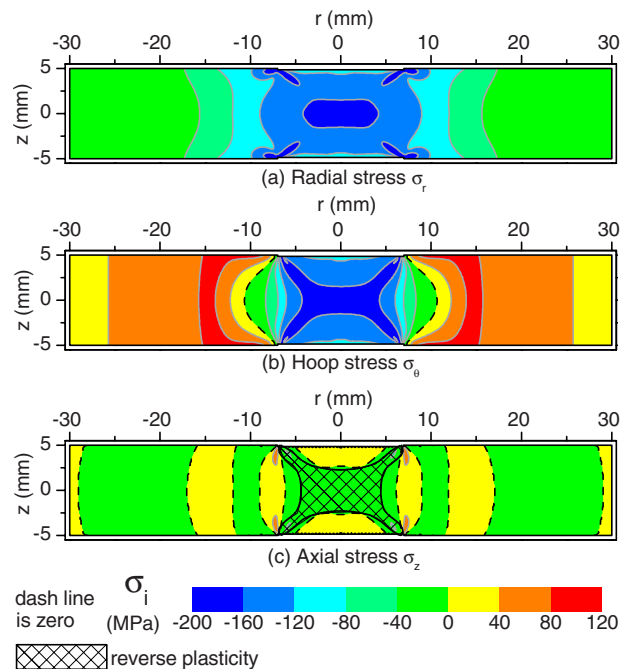
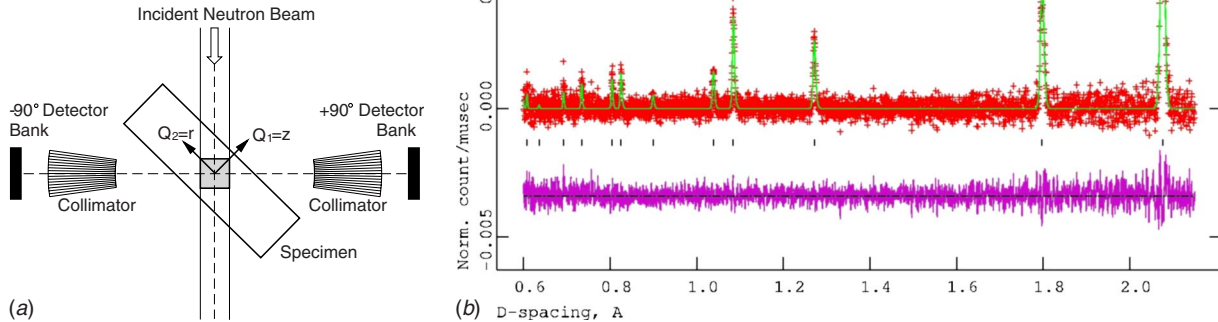


Fig. 9 Finite element model prediction of the radial, hoop, and axial residual stresses along the diameter plane using the ABAQUS combined hardening model of the 316L stainless steel. The cross hatched region in (c) is where the reverse plasticity is.



**Fig. 10 Schematic setup of SMARTS for spatially resolved measurements, and (b) typical diffraction pattern. The crosses on are the data, the line through the data is the Rietveld refinement fit, and below those is the difference curve. The tick-marks indicate the positions of the face-centered cubic peaks.**

scans the axial strains  $\varepsilon_z$  were measured in the +90 degrees bank. Further measurements were also executed on an unindented, annealed disk (disk C).

A typical diffraction pattern for the 316L stainless steel from this study is shown in Fig. 10(b). Many peaks from the austenitic stainless steel are present enabling Rietveld full pattern analysis [20]. Being able to use multiple peaks in the refinement greatly improves the statistics, and using the GSAS software [21] we can determine the lattice parameter  $a$  of the  $fcc$  crystal structure with a relative accuracy of about  $50 \times 10^{-6}$  or  $50 \mu\epsilon$ , using count times on the order of 20 min for the  $8 \text{ mm}^3$  sampling volumes.

The lattice strains are calculated based on a stress-free reference measurement. In this case the average stress-free lattice parameters from a series of measurements on three small cubes ( $5 \times 5 \times 5 \text{ mm}^3$ ) were determined. Then the residual strains can be calculated as follows:

$$\varepsilon_i = \frac{a_i}{a_i^0} - 1 \quad i = r, \theta, z \quad (5)$$

where  $a_i$  and  $a_i^0$  are the stresses and unstressed lattice parameters, respectively, in the test specimen and in the stress-free cubes along the different directions ( $r$ ,  $\theta$ , and  $z$ ). Then the residual stress components were evaluated using Hooke's law as follows:

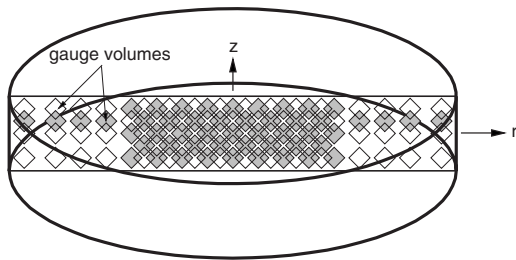


**Fig. 11 Location of gauge volumes ( $2 \times 2 \times 2 \text{ mm}^3$ ) for the neutron measurements. Some gauge volumes are colored gray in order to distinguish overlapping volumes.**

$$\sigma_i = \frac{E(1-\nu)}{(1+\nu)(1-2\nu)} \left[ \varepsilon_i + \frac{\nu}{1+\nu} (\varepsilon_j + \varepsilon_k) \right] \quad i, j, k = r, \theta, z \quad (6)$$

where  $E$  is the elastic modulus, and  $\nu$  is Poisson's ratio.

## 7 Contour Method

The residual hoop stresses on a diametrical plane of two disks (disks A and B) indented under the same experimental conditions were measured with the contour method. Disk A was the same scanned by neutron diffraction and was cut in half along the scanned plane using wire EDM and a  $50 \mu\text{m}$  diameter tungsten wire. Because of errors attributed to the thin wire, disk B was cut using a  $100 \mu\text{m}$  diameter brass wire. Both disks were submerged in temperature-controlled de-ionized water throughout the cutting process. "Skim cut" settings were used. The disks were constrained by clamping on both sides of the cut to the work plate of the EDM machine. To prevent any thermal stresses, the specimens and the fixture were allowed to come to thermal equilibrium in the water tank before clamping. The clamping direction was parallel to the wire axis. As controls, two unindented disks were cut using the  $50 \mu\text{m}$  and  $100 \mu\text{m}$  diameter wire, respectively.

After cutting, disk A was removed from the clamping fixture. The contours of both cut surfaces were measured using a Taylor-Hobson Talyscan 250 laser scanner. A laser triangulation probe of 2 mm range and resolution of  $0.1 \mu\text{m}$  was used. The cut surfaces were measured on a  $0.1 \text{ mm}$  spaced grid, giving about 60,000 points on each cut surface. The measured shapes are not plotted here because of space limitations but are available elsewhere [22]. The peak-to-valley amplitude of the contour is about  $40 \mu\text{m}$ . The primary shape of the contour is high in the center of the disk and lower at the diameter edges. Disk B was measured using the laser scan machine described before [23]. The surfaces were scanned using rows separated by  $0.1 \text{ mm}$  in the axial direction  $z$ , with data points within a row sampled every  $0.04 \text{ mm}$ , giving about 113,000 points on each cut surface.

The cut surfaces of the two unindented disks were also measured using the two laser scan machines mentioned above. The contour of the unindented disk that was cut using the  $100 \mu\text{m}$  brass wire was flat to within measurement resolution. The contour of the unindented disk that was cut using the  $50 \mu\text{m}$  tungsten wire was higher by about  $6 \mu\text{m}$  on the top and bottom edges of

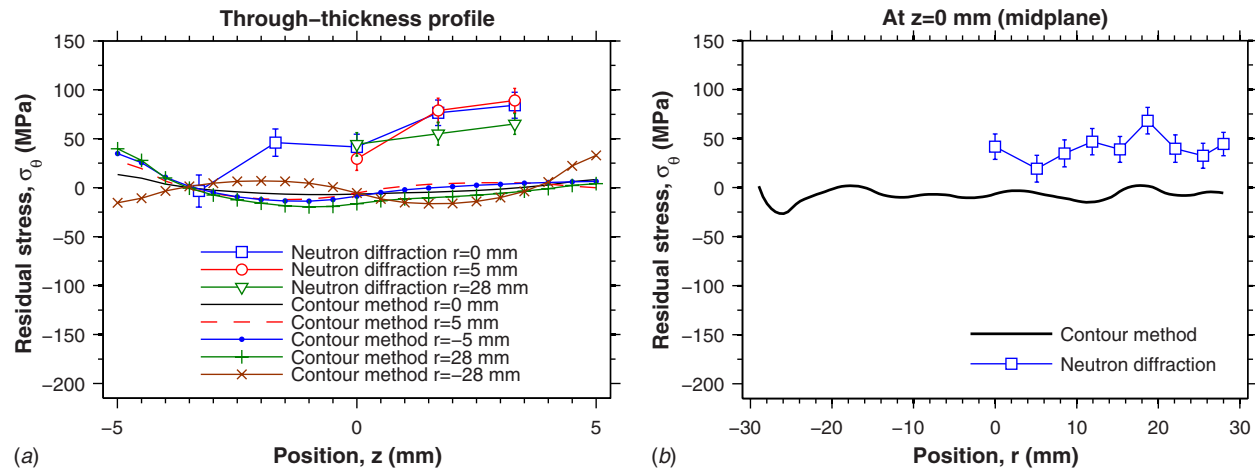


Fig. 12 Residual stress measured with the contour method and neutron diffraction on unindented disks of the stress-relieved 316L steel

the 10 mm thickness than in the midplane. Recall that slitting test on the annealed 316L material indicated that the postannealing stresses were less than 10 MPa. Therefore, this contour is probably caused by the EDM cutting and not by residual stress since it would require stresses over 100 MPa to produce such a contour. In fact, the wire used had half the diameter of the smallest wire previously reported for contour measurements. Hence, in order to correct this effect the contour on the unindented disk was subtracted from the contour of the indented disk A, which was cut with the same wire.

The hoop stresses that were originally present on the plane of the cut of each disk were calculated numerically by elastically deforming the cut surface into the opposite shape of the contour that was measured on the same surface [24]. This was accomplished using a 3D elastic FE model. A model was constructed of one-half of the disk. The mesh used 51,920 linear hexahedral eight-node elements with reduced integration (C3D8R). The material behavior was considered elastically isotropic with an elastic

modulus of 193 GPa and Poisson's ratio of 0.3. The raw data were processed into a form suitable to calculate stresses using a procedure described in detail elsewhere [23]. The data from each half were interpolated onto a common grid and then averaged to remove several potential error sources. In order to smooth out noise in the measured surface data and to enable evaluation at arbitrary locations, the data were fitted to a bivariate smoothing spline. The smoothing spline fits were evaluated at a grid corresponding to the FE nodes, and those values at the nodal locations were then used as displacement boundary conditions in the direction normal to the cut surface.

## 8 Results and Discussion

The stress measurements on the unindented disks of the stress-relieved 316L steel, which had been independently measured to have stress magnitudes below 10 MPa, indicate resolution limits for the measurement methods. In Fig. 12, the contour results from the test cut with 100  $\mu$ m diameter wire are plotted at the locations of the neutron measurements for comparison purposes. The contour results are generally less than  $\pm 20$  MPa except at isolated

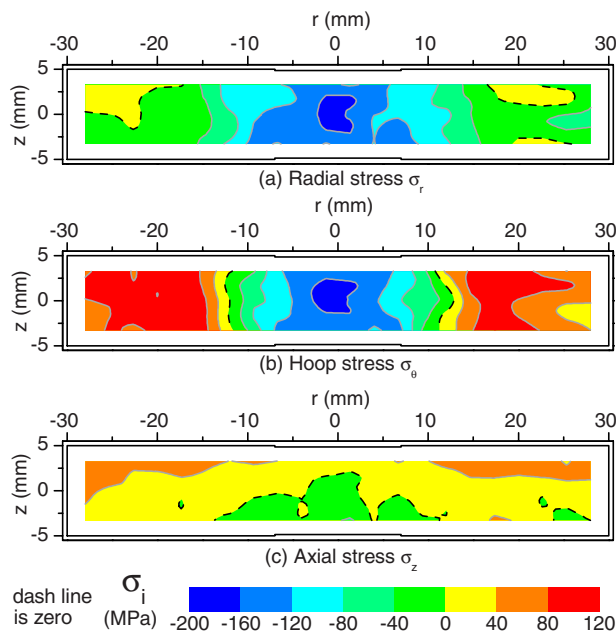


Fig. 13 Maps of (a) radial, (b) hoop, and (c) axial residual stresses measured with neutron diffraction on the diametrical plane

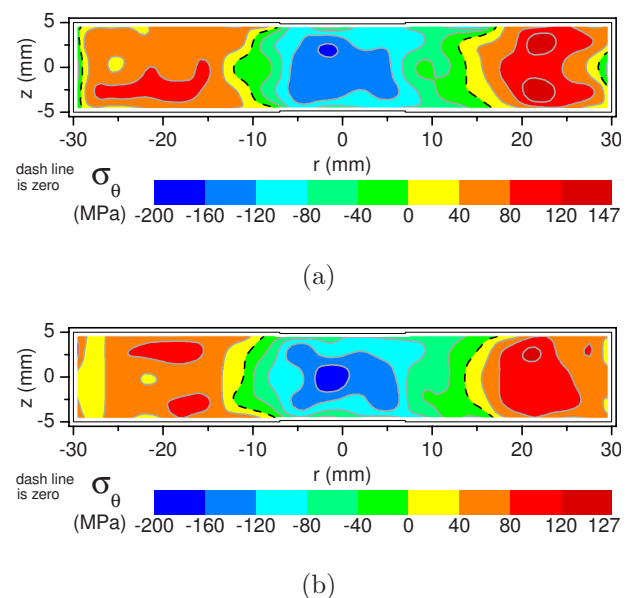


Fig. 14 Residual hoop stress map measured with the contour method along the diameter plane for (a) disk A and (b) disk B

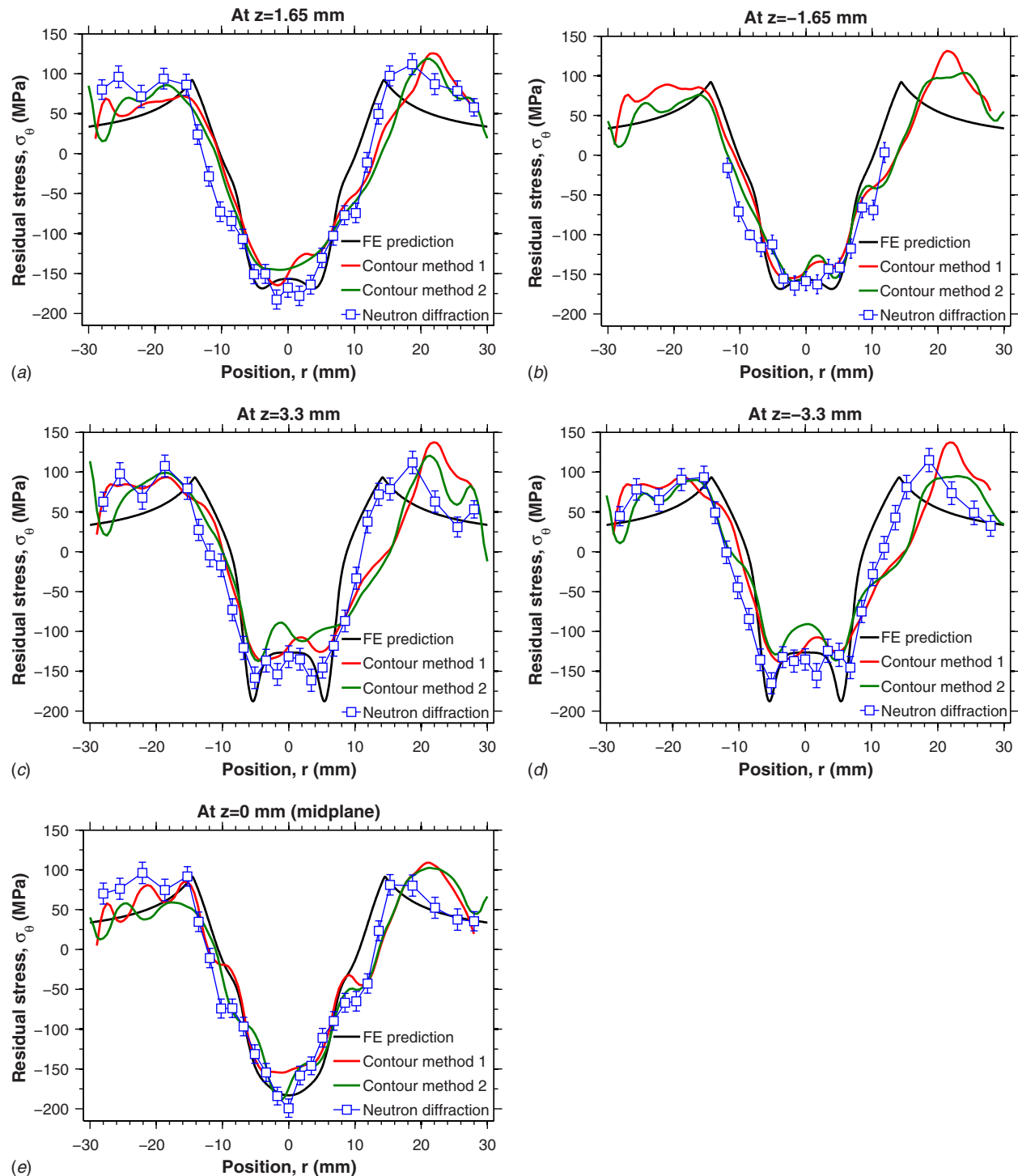


Fig. 15 Hoop residual stresses measured with neutron diffraction and contour method compared with the FE prediction

regions near the edges. The contour results on the disk cut with the 50  $\mu\text{m}$  diameter wire are not plotted but exceed 100 MPa, illustrating the importance of testing before using unproven cutting conditions. The neutron results average over 40 MPa in tension with the unstressed lattice parameters that were determined carefully from measurements on three small cubes taken from the stress-relieved plate. Subsequent neutron results were not corrected to choose a more favorable value for unstressed lattice spacing because that would be an a posteriori adjustment based on assumed knowledge about the results.

The experimental measurements on the indented disks agree with each other and the FE model within the experimental resolution limits, indicating the suitability of these validation specimens. Figures 13 and 14 show stress maps measured by neutron diffraction and the contour method, respectively, for comparison with the FE-model stress maps of Fig. 9. Figures 15 and 16 show line plots extracted from the stress maps. The FEM results are point wise stress values. Based on the stress gradients, the effects of averaging over the sampling volume are estimated to be less than  $\pm 5$  MPa. The overall agreement is quite good. The most



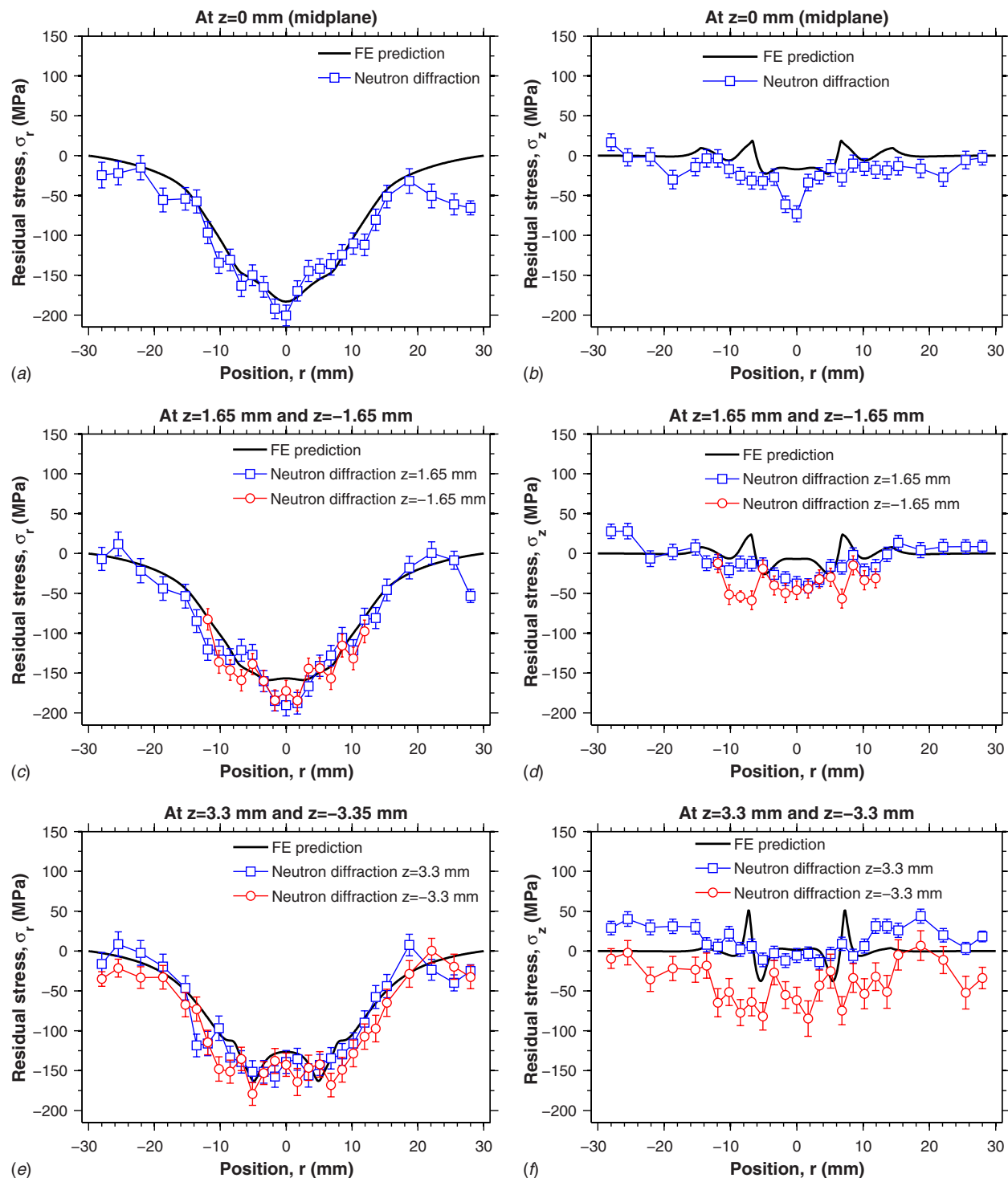


Fig. 16 Radial and axial residual stresses measured with neutron diffraction compared with the FE prediction

obvious discrepancies appear in the low magnitude axial stresses where apparent errors in unstressed lattice spacing shift the entire profile.

Root mean square (rms) averages of the differences between hoop stress values from Fig. 15 were calculated and are given in Table 1. To better interpret the results for possible measurement on other materials, values are also given in microstrain because strain or deformation is a better measure of the sensitivity of the measurement methods. The best agreement is between the two contour measurements at about 20 MPa or 100  $\mu\epsilon$ , which is excellent repeatability. The neutron diffraction agrees with both con-

Table 1 Root mean square difference between pairs of hoop stress measurements or the finite element model, over the neutron diffraction measurement locations (Note that the microstrain ( $\mu\epsilon$ ) equivalent of the values are provided in parenthesis)

	Contour 2 (MPa)	Neutron (MPa)	FE model (MPa)
Contour 1 (MPa)	20 (104)	27 (140)	32 (166)
Contour 2 (MPa)	—	28 (145)	33 (171)
Neutron (MPa)	—	—	33 (171)

tour measurements to about 28 MPa or 145  $\mu\epsilon$ , which is also in excellent agreement especially considering the results in the undented disks. The finite element model agrees with all three of the measurements within about 33 MPa or 170  $\mu\epsilon$ , which is still in very good agreement when comparing with a model. Neither experimental method resolves some of the finer feature of the FE prediction, such as the X-shaped peak compressive stress region for the hoop stress. Therefore, such detail in the FE model cannot be considered to be experimentally validated.

Modeling the material hardening under reverse loading conditions appears to be the limiting factor in the fidelity of the FE model, and it could be improved. Figure 8 showed the sensitivity of the modeled residual stresses to the hardening model. The hardening model was calibrated using data only from symmetric strain-controlled cyclic experiments with a strain range  $\Delta\epsilon$  of 4% (2% of true strain in compression followed by a 2% of true strain in tension). More calibration data with different strain amplitudes could improve the model since local regions of the disks see up to 5% plastic strain and other regions see less than 2%. Other modeling assumptions likely have less effect. Changing the friction coefficient from 0.0 to 0.2 changed the stresses by less than 25 MPa at the measurement locations plotted in Fig. 15. The maximum heating from plastic work was estimated by a conservative adiabatic FE analysis to be 5 K, which would only be expected to lower the yield stress by about 0.1% based on the temperature dependence of the shear modulus [25].

Some experimental conditions also affected the accuracy of the predictions. The measurement of the indentation footprint indicated that the thickness reduction may have differed from perfect axisymmetry by about 4%. The resulting effect on stresses is not easily estimated. The asymmetry may have occurred because of imperfect colinearity of the two indenters. A tighter parallel tolerance on the indentation surface relative to the opposite surface of the indenter (the one loaded by the machine) might improve that colinearity. However, a more error tolerant design, such as a radius used rather than flat indenter surface, would probably be more productive.

The type of EDM wire used probably led to the need to correct the contour of disk A based on the contour of a cut in a stress-free disk. This demonstrates the importance of always making a control cut in a stress-free material. The wire used on disk A was, at 50  $\mu\text{m}$ , half the diameter of the one used on disk B and it was also tungsten as compared with brass. There is not sufficient information to tell which difference caused the cut to be nonflat even in a stress-free disk. The only previous time such a correction was necessary in the authors' experience was for a 100  $\mu\text{m}$  brass wire that was unusual in that it was zinc-coated [24]. However, we note that other unpublished measurements using the small tungsten wire have been quite successful. The use of a small wire can be advantageous because some error sources are reduced with a thinner cut.

Comparing the two contour method measurements demonstrates not only repeatability of the method but also has important implications for more complicated parts. The rms difference between the two contour results of 20 MPa or 0.01% of  $E$  would be quite good and comparable to other methods if the measurements had been performed under identical experimental conditions. Since the cut on disk A used a different EDM wire and required a correction of up to 50 MPa based on the cut made on stress-free disk, the agreement is more impressive. For this specimen, the correction could have been avoided by better choice of the cutting wire based on stress-free testing. However, in parts with a more complicated cross section, such errors may be present no matter the cutting conditions because the width of the EDM cut will change slightly as the thickness of the part changes during the cut. Based on the results of the measurements on the two disks, a correction based on a cut in a stress-free part could successfully correct for such errors.

## Acknowledgment

Much of this work was performed at the Los Alamos National Laboratory, operated by the Los Alamos National Security, LLC for the National Nuclear Security Administration of the U.S. Department of Energy under Contract No. DE-AC52-06NA25396. This work has benefited from the use of the Lujan Neutron Scattering Center at Los Alamos Neutron Science Center, which is funded by the Department of Energy's Office of Basic Energy Sciences. Mr. Pagliaro's work was sponsored by a fellowship from the Università degli Studi di Palermo. The authors would like to thank Professor Michael Hill at U.C. Davis for the scanning of the surface contours.

## References

- [1] Withers, P. J., 2007, "Residual Stress and Its Role in Failure," Rep. Prog. Phys., **70**(12), pp. 2211–2264.
- [2] Hill, M. R., DeWald, A. T., Rankin, J. E., and Lee, M. J., 2005, "Measurement of Laser Peening Residual Stresses," Mater. Sci. Technol., **21**(1), pp. 3–9.
- [3] Hatamleh, O., Lyons, J., and Forman, R., 2007, "Laser Peening and Shot Peening Effects on Fatigue Life and Surface Roughness of Friction Stir Welded 7075-T7351 Aluminum," Fatigue Fract. Eng. Mater. Struct., **30**(2), pp. 115–130.
- [4] Woo, W., Choo, H., Prime, M. B., Feng, Z., and Clausen, B., 2008, "Microstructure, Texture and Residual Stress in a Friction-Stir-Processed Az31b Magnesium Alloy," Acta Mater., **56**(8), pp. 1701–1711.
- [5] Withers, P. J., Turski, M., Edwards, L., Bouchard, P. J., and Buttle, D. J., 2008, "Recent Advances in Residual Stress Measurement," Int. J. Pressure Vessels Piping, **85**(3), pp. 118–127.
- [6] Martineau, R. L., Prime, M. B., and Duffey, T., 2004, "Penetration of HSLA-100 Steel With Tungsten Carbide Spheres at Striking Velocities Between 0.8 and 2.5 km/s," Int. J. Impact Eng., **30**(5), pp. 505–520.
- [7] Prime, M. B., Gnäupel-Herold, T., Baumann, J. A., Lederich, R. J., Bowden, D. M., and Sebring, R. J., 2006, "Residual Stress Measurements in a Thick, Dissimilar Aluminum Alloy Friction Stir Weld," Acta Mater., **54**(15), pp. 4013–4021.
- [8] Kelleher, J., Prime, M. B., Buttle, D., Mummery, P. M., Webster, P. J., Shackleton, J., and Withers, P. J., 2003, "The Measurement of Residual Stress in Railway Rails by Diffraction and Other Methods," J. Neutron Res., **11**(4), pp. 187–193.
- [9] DeWald, A. T., and Hill, M. R., 2006, "Multi-Axial Contour Method for Mapping Residual Stresses in Continuously Processed Bodies," Exp. Mech., **46**(4), pp. 473–490.
- [10] Pagliaro, P., Prime, M. B., and Zuccarello, B., 2006, "Multi Stress Components From Multiple Cuts for the Contour Method," *Proceedings of the 35 AIAS Conference*, Università Politecnica delle Marche, Ancona, Italy.
- [11] Mahmoudi, A. H., Stefanescu, D., Hossain, S., Truman, C. E., Smith, D. J., and Withers, P. J., 2006, "Measurement and Prediction of the Residual Stress Field Generated by Side-Punching," ASME J. Eng. Mater. Technol., **128**(3), pp. 451–459.
- [12] Korsunsky, A. M., Liu, J., Golshan, M., Dini, D., Zhang, S. Y., and Vorster, W. J., 2006, "Measurement of Residual Elastic Strains in a Titanium Alloy Using High Energy Synchrotron X-Ray Diffraction," Exp. Mech., **46**(4), pp. 519–529.
- [13] Ezeilo, A. N., and Webster, G. A., 2000, "Neutron Diffraction Analysis of the Residual Stress Distribution in a Bent Bar," J. Strain Anal. Eng. Des., **35**(4), pp. 235–246.
- [14] Cheng, W., and Finnie, I., 2007, *Residual Stress Measurement and the Slitting Method*, Springer Science+Business Media, LLC, New York.
- [15] Schajer, G. S., and Prime, M. B., 2006, "Use of Inverse Solutions for Residual Stress Measurements," ASME J. Eng. Mater. Technol., **128**(3), pp. 375–382.
- [16] Lemaitre, J., and Chaboche, J.-L., 1990, *Mechanics of Solid Materials*, Cambridge University Press, Cambridge.
- [17] Choteau, M., Quaegebeur, P., and Degallaix, S., 2005, "Modelling of Bauschinger Effect by Various Constitutive Relations Derived From Thermodynamical Formulation," Mech. Mater., **37**, pp. 1143–1152.
- [18] 2006, *ABAQUS User's Manual, Version 6.6*, ABAQUS Inc., Pawtucket, RI.
- [19] 2006, *ABAQUS Theory Manual Version 6.6*, ABAQUS Inc., Pawtucket, RI.
- [20] Von Dreele, R. B., 1997, "Quantitative Texture Analysis by Rietveld Refinement," J. Appl. Crystallogr., **30**, pp. 517–525.
- [21] Larson, A. C., and Von Dreele, R. B., 1986, "General Structure Analysis System (GSAS)," Los Alamos National Laboratory, Los Alamos, NM, Tech. Report No. LA-UR-86-748.
- [22] Pagliaro, P., 2008, "Mapping Multiple Residual Stress Components Using the Contour Method and Superposition," Ph.D. thesis, Università degli Studi di Palermo, Palermo, Italy.
- [23] Prime, M. B., Sebring, R. J., Edwards, J. M., Hughes, D. J., and Webster, P. J., 2004, "Laser Surface-Contouring and Spline Data-Smoothing for Residual Stress Measurement," Exp. Mech., **44**(2), pp. 176–184.
- [24] Prime, M. B., 2001, "Cross-Sectional Mapping of Residual Stresses by Measuring the Surface Contour After a Cut," ASME J. Eng. Mater. Technol., **123**(2), pp. 162–168.
- [25] Chen, S. R., 2007, private communication.